Calibration of Fluorescence Resonance Energy Transfer in Microscopy Using Genetically Engineered GFP Derivatives on Nickel Chelating Beads

Douglas C. Youvan, Christopher M. Silva, Edward J. Bylina,
William J. Coleman, Michael R. Dilworth, and Mary M. Yang*

*Corresponding Author:

KAIROS Scientific Inc.
Bldg. 62
3350 Scott Blvd.
Santa Clara, CA 95054 USA

E-mail: myang@kairos-scientific.com

Website: www.kairos-scientific.com

Received: 9/5/97

Accepted: 9/18/97

Ad Hoc Editor: Professor George Phillips

Abstract

Molecular reagents, software algorithms, and optics are described for calibrating an epifluorescence microscope for fluorescence resonance energy transfer (FRET) imagery. This *MicroFRET* system compensates for overlap among donor, acceptor, and FRET spectra. The effectiveness of this new method relies on the use of well characterized fluorescent beads as standards in conjunction with radiometrically calibrated image processing techniques. To calibrate the system, three bead types (bearing pure donor, pure acceptor, and a donor-plus-acceptor FRET mix) are imaged sequentially by three epifluorescence cubes that are fabricated to maintain proper optical image registration. A series of algorithms corrects and combines the three monochrome images into one RGB image in which FRET, acceptor, and donor fluorescence are pseudocolored red, green, and blue, respectively. The utility of this new method is demonstrated on samples exhibiting FRET between genetically engineered derivatives of the Green Fluorescent Protein (GFP) bound to the surface of Ni chelating beads by Histidine-tags. In addition, various theoretical models are considered for conformational differences in FRET pairs on the bead surface.

Introduction

Fluorescence resonance energy transfer (FRET) is a non-radiative process whereby energy from a fluorescent donor molecule is transferred to a fluorescent acceptor without the involvement of a photon (Förster, 1948,1959). One result of this interaction is that excitation of the donor molecule enhances the fluorescence emission of the longer-wavelength acceptor molecule (i.e., sensitized acceptor emission). The quantum yield of the donor fluorescence emission is concomitantly diminished. The reason that FRET has become a valuable tool for microscopy is that the efficiency of energy transfer has a strong inverse dependence on the distance between the donor and acceptor. Thus, the appearance of FRET is a highly specific indicator of the proximity of the two molecules. This led to the idea of using FRET efficiency as a "spectroscopic ruler" to measure molecular distances (Stryer, 1978).

The Förster Equations. The basic equations describing this type of energy transfer involve expressions for the energy transfer rate constant, the transfer efficiency, the so-called Förster radius or critical distance (R_0, in cm), the spectral overlap integral, and the normalized fluorescence emission spectrum of the donor. For randomly oriented molecules separated by a distance r, when $r = R_0$, the efficiency of energy transfer is 50%, and the donor fluorescence lifetime is reduced by a factor of 2. Values of R_0 are on the order of tens of Ångstroms. FRET efficiencies fall-off at an inverse 6^{th} power of distance as normalized by R_0. Doubling the distance between donor and acceptor molecules from R_0 to $2R_0$ decreases the FRET efficiency from 50% to less than 1% because of the inverse-6^{th} power dependence: $(0.5)^6$. Thus FRET is a very useful tool for determining whether two molecules are in close proximity. This is especially true in the case of interacting macromolecules, where molecular radii are similar in size to the actual R_0 values of their fluorescent tags. [The Förster equations and a more complete description of variables affecting FRET are given in the Appendix, along with original literature citations.]

Limitations of FRET Microscopy. A typical FRET experiment for observing cells involves specifically labeling particular molecules with fluorescent dyes and detecting these dyes over selected excitation and emission wavelength ranges. These wavelength ranges are commonly referred to as 'channels' for a particular fluorophore. Fluorescent labeling is easier to accomplish for extracellular molecules than for intracellular ones. In the latter case, the dye-conjugated molecules must be injected into the cell for observation, or, alternatively, the labeled molecules may be overlaid onto a thin section of fixed, permeabilized tissue. Recently, however, the availability of green fluorescent protein (GFP) mutants with shifted excitation and emission spectra has made it feasible to measure protein-protein interactions by using GFP tags as intracellular markers (Prasher *et al*., 1992; Heim *et al*., 1994; Cubitt *et al*., 1995; Youvan & Michel-Beyerle, 1996; Cormack *et al*., 1996; Lossau *et al*., 1996). These protein chimeras are expressed intracellularly and do not require any chemical treatment to become fluorescent. FRET between fusions of blue- and green-emitting GFP variants has been reported (Mitra *et al*., 1996).

Although FRET microscopy has the potential to become a widely used analytical tool in these systems, accurate steady-state measurement of FRET by standard epifluorescence microscopy has been hindered by several limitations (Jovin & Arndt-Jovin, 1989). These limitations apply to GFP as well as to other fluorescent FRET pairs:

1) Bleed-through or contributions of donor (and isolated acceptor) fluorescence emission into the FRET channel due to spectral overlap must be compensated by using accurate calibration standards.
2) To correct for (1), multiple images taken over different excitation and emission wavelength ranges must be acquired and image registration maintained throughout, so as to allow pixel by pixel corrections.
3) Photobleaching of the donor during the measurement will result in anomalously low estimates of FRET in the sample.

Because of recent advances in ‘chromosome painting’, cell biologists are becoming familiar with epifluorescence microscopes that utilize multi-bandpass filters to obtain information on several dyes simultaneously. Some of these instruments employ interferometry (Schrock *et al*., 1996), while others use filter wheels in the excitation path to select specific excitation bands. In both cases, an assumption is made that excitation at a given wavelength results in emission from the next reddest transmission band (Fig. 1). While multiband cubes help to solve the image registration problem for separable dyes, fluorescence phenomena which involve large or variable Stokes shifts can not be addressed. Multiband systems can not be used to detect FRET because the FRET emission channel is not the next (redder) emission band, and it is therefore indistinguishable from the donor's emission.

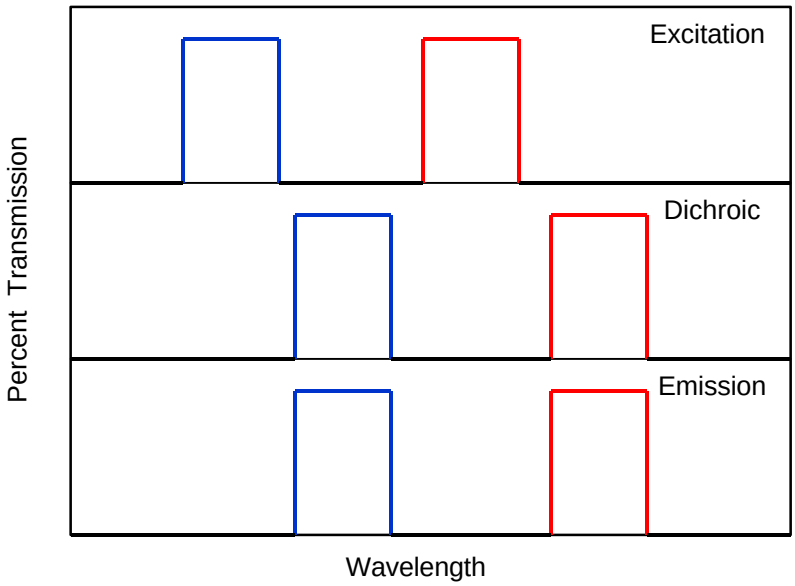

Figure 1. Double-band epifluorescence filter cube transmission characteristics. Channel 1 (blue) and channel 2 (red) can be engineered to discriminate between two different fluorophores. Multiband epifluorescence cubes can not be used for FRET analysis, because the emission of an uncoupled donor is indistinguishable from the sensitized emission of a FRET acceptor.

The method described in this paper utilizes three separate epifluorescence cubes. Image registration problems are minimized by careful selection and measurement of the dichroic and emission filters' optical properties. Calibration parameters obtained from tagged beads can be applied to other images where the conditions under which the images are acquired are identical. This new design also makes it feasible to detect relatively small amounts of FRET within a given pixel, because the mathematical correction is much simpler (and therefore more accurate) than was previously possible.

Materials and Methods

Fluorescent Proteins and Beads. Two derivatives of GFP were selected for FRET standards based on their spectral properties. The mutant BFP11, constructed using combinatorial mutagenesis, contains the mutations F64M/Y66H (Lossau *et al*., 1996) and is similar to the mutant of Heim *et al*. (1994). It has blue-shifted excitation and emission maxima relative to wild-type GFP (Fig. 2 and Table 1 below). The mutant RSGFP4 (Delagrave *et al*., 1995), generated by combinatorial mutagenesis, contains the mutations F64M / S65G / Q69L. RSGFP4 has spectral properties similar to the S65T mutant also reported by Heim *et al*. (1994). As the acceptor in a FRET pair, both S65T and RSGFP4 are superior to other red-shifted excitation mutants such as RSGFP8 (F64L + S65T), because the latter mutant has significant excitation in the violet (Cormack *et al*., 1996).

BFP11 and RSGFP4 were engineered to include His_6 tags on their amino-termini to facilitate protein purification and later attachment on Ni-Sepharose beads. The proteins were expressed in *E. coli* strain BL21 (DE3) and grown for 24 hours in 2×YT medium containing 25

μg ml^{-1} kanamycin and 10 μM IPTG. Cultures were grown at 27° C with shaking. After harvesting, the cells were pelleted at 5,000 × g for 5 min and resuspended in cold lysis buffer consisting of 20 mM Tris-HCl (pH 8.0), 100 mM NaCl, 1 mM PMSF, 1 μg ml^{-1} pepstatin A, and 1 μg ml^{-1} leupeptin. The cells were ruptured in an ice-cold French press at 20,000 psi and collected in centrifuge tubes on ice. After centrifugation for 30 min at 35,000 × g, the supernatant was applied to a Novagen HisBind purification column, according to the manufacturer's instructions. The bound proteins were eluted in 1 M imidazole and dialyzed four times against a 100-fold dilution of buffer containing 50 mM Tris-HCl (pH 8.0) to remove the imidazole. The final protein concentration was determined by a Bradford assay (Bio-Rad). An SDS-PAGE gel was run to confirm the purity and size of the dialyzed fraction (data not shown). Fluorescence excitation and emission spectra were recorded on a Photon Technology QM-1 fluorimeter.

GFP-coated bead standards were prepared using the following method. HiTrap metal chelating Sepharose beads were charged according to the manufacturer's (Pharmacia Biotech) instructions by washing the beads with 50 mM $NiSO_4$. Pharmacia describes these beads as highly cross-linked agarose to which imino-diacetic acid has been coupled by stable ether groups via a seven-atom spacer arm. The beads were then washed extensively with 50 mM Tris-HCl (pH 8.0) to remove traces of uncomplexed Ni ions. A mixture was made of purified BFP11 and RSGFP4 proteins (2:1 molar ratio, respectively) at total protein concentration of approximately 0.4 mg ml^{-1} in 50 mM Tris-HCl buffer to avoid heterodimer formation prior to attachment to the beads. This was confirmed by measuring this mixture of the proteins in a fluorimeter and examining the spectra for any indications of FRET. 1.5 ml of this mixture was added to 50 μl of a bead slurry and incubated on ice for 1 hour with frequent mixing. Excess protein ensures that the beads were fully loaded. To remove nonspecifically bound protein (if any) the suspension was washed twice with a buffer containing 5 mM imidazole, 0.5M NaCl and 20 mM Tris-HCl, followed by one wash with 50 mM Tris-HCl. All washes were done by centrifuging the beads at 1,000 × g for 30 s in a microcentrifuge and resuspending the pellet in the appropriate buffer. BFP-11 (donor) beads and RSGFP4 (acceptor) beads were prepared in the same way. The mean particle size of the beads is approximately 34 μm.

To confirm that the fluorescence emission from the FRET bead is actually FRET, as well as to ensure that the spectral properties of the two GFP variants have not changed as a result of binding to the Sepharose beads, we treated a sample of each type of bead with imidazole, which releases the protein. Fluorescence excitation and emission spectra of each bead slurry were obtained before and after treatment with imidazole. Fig. 2a shows donor and acceptor bead spectra before treatment. These spectra are virtually indistinguishable from those of the corresponding purified proteins in solution. Fluorescence emission spectra for the FRET beads are shown in Fig. 2b. The thick line shows the emission spectrum of a suspension of FRET beads excited at 370 nm. The thin line shows the emission spectrum of the same beads after both RSGFP4 and BFP11 have been released from the beads by treatment with imidazole. The decreased donor emission and enhanced acceptor emission are characteristic of FRET. This effect is reversed when the two proteins are released from the beads.

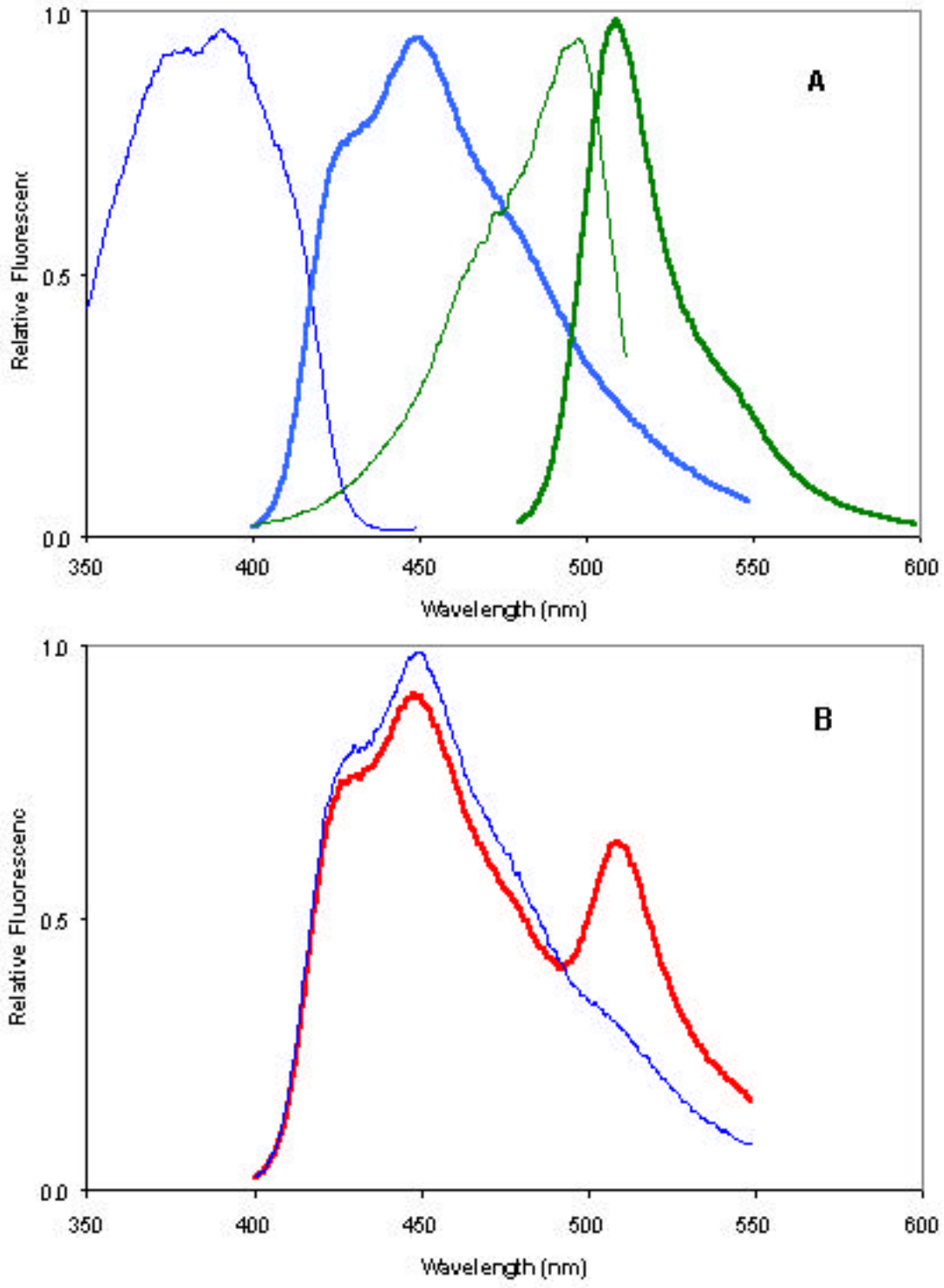

Figure 2. Panel A: Fluorescence excitation (thin lines) and emission (thick lines) spectra of BFP11 (blue) and RSGFP4 (green) proteins attached to chelating Sepharose beads via their His tags. Panel B: Comparison between the fluorescence emission of the BFP11 and RSGFP4 FRET pair bound (red) and following release (blue) from chelating beads.

Instrumentation and Software. The *MicroFRET* instrument is based on an Olympus BX60 (upright) or IX70 (inverted) epifluorescence microscope. The detection system uses a KAIROS Peltier-cooled CCD camera (Model K7: 16 bit, 760 × 510 resolution, or Model K8: 16 bit, 1340 x 1037 resolution) coupled to the microscope's trinocular port. The CCD camera coupling to the microscope is made through a c-mount to Olympus U-PMTVC and Olympus U-SPT relay tubes (containing a 2.5 x projection eyepiece). The threaded U-PMTVC mount can be adjusted to make the CCD camera parfocal with the oculars. Other hardware components used in this study include: 10X/0.40 objective (U-plan apo infinity / 0.17) and a 75 watt QTH light source.

Epifluorescence cube specifications are given in Table 1, below. Because image registration and distortion is highly dependent on exact surface parallelism within the dichroic and emission filters' surfaces, we have measured the dichroic and emission filters of all three cubes for surface parallelism (using an autocollimator) and for surface flatness (using an interferometer) to be less than or equal to 15 arc seconds of wedge parallelism and approximately 10 waves flatness.

Camera control, image display, and data processing are all performed using *MicroFRET* software developed in-house using C++ and MFC. Algorithms for background subtraction, spectral overlap corrections, and transformation of data from the three GFP channel basis set into a color space defined by the primary colors of red, green, and blue are included. This latter process produces an enhanced image in which FRET, acceptor, and donor pixels are more clearly differentiated and pseudocolored accordingly. In addition, a suite of image processing functions for both 16-bit monochrome and 24-bit RGB images are available. This software currently runs under MS Windows.

Results

Image Acquisition of GFP-Labeled Beads. Three monochrome images were acquired using the set of three epifluorescence cubes to image a mixture of three different types of fluorescent beads (described in Table 1). The epifluorescence cubes and bead types are labeled Donor, Acceptor, and FRET to emphasize that the cubes and beads are spectrally matched. The donor bead carries a GFP derivative (BFP11) with an excitation maximum in the long wave UV and emission in the blue. The acceptor bead carries RSGFP4, which is excited maximally in the cyan and fluoresces in the green. These excitation and emission wavelengths are matched to the donor and acceptor cubes. The FRET bead carries both the blue and green GFP derivatives, and the corresponding FRET cube is optimized to excite the blue donor and image the green acceptor after energy transfer has occurred. Images acquired using the Donor, Acceptor, and FRET cubes are referred to as the D1, A1, and F1 images, respectively.

Cube	Excitation	Dichroic	Emission
Donor	335 – 380	410	435 – 490
Acceptor	450 – 490	495	505 – 550
FRET	335 – 380	410	505 – 720

Bead / Derivative	Excitation	-----	Emission
Donor / BFP11	380	-	445
Acceptor / RSGFP4	490	-	510
FRET / BFP11+RSGFP4	380	-	510

Table 1. Spectral characteristics of epifluorescence cubes and fluorescent beads used in this work. Wavelengths (nm) are given as λ_{max} for beads, as cut-on and cut-off (50% peak transmission) for excitation and emission filters, and as the inflection point for dichroic filters.

Spectral mixing among the donor, acceptor, and FRET beads can be observed in the spatially coregistered monochrome and RGB images of Fig. 3. In the D1 image, we see that the donor beads are the brightest, but dimmer FRET beads are also observed. In the A1 image, we see that the acceptor beads are the brightest, but dimmer FRET beads are also observed. In the F1 image, we see that the FRET beads are the brightest, but dimmer donor beads are observed. This is consistent with the fluorescence spectra shown in Fig. 2 and the parameters given in Table 1. The pseudocolored, upper left image (RGB1) in Fig. 3 is the result of encoding the pixel values of each of these monochrome images into an intensity value for each of the red, green and blue components of the image. F1 is loaded into the red color channel, A1 is loaded into the green color channel and D1 is loaded into the blue color channel. Because of spectral overlap, the various bead types are not visually distinct or well defined in this RGB image.

Careful observation of the emission spectra of the donor and the acceptor shows that there is no wavelength where the two fluorophores can be separated. For example, the use of a very narrow bandpass emission filter at 550 nm would not only fail to separate the two fluorophore's emissions, but it would also result in the loss of most of the microscope's light gathering ability. Using higher intensity illumination to compensate for this loss is likely to result in photobleaching. In contrast, we have selected broad-band emission filters and a relatively low intensity excitation source.

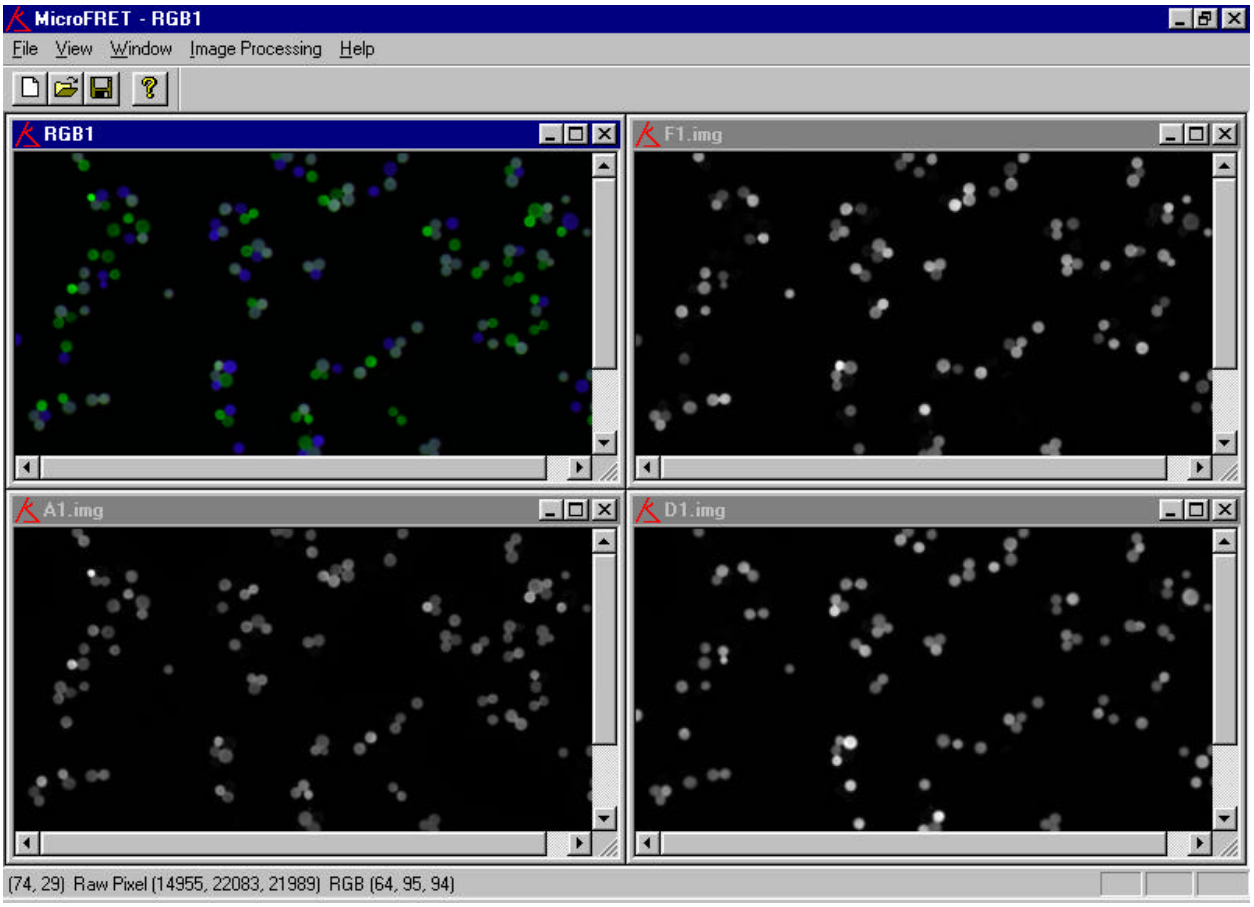

Fig. 3. *MicroFRET* graphical user interface showing three monochrome images taken of the bead mixture using the donor, acceptor, and FRET epifluorescence cubes described in Table 1. These images have been combined to produce an RGB image which does not fully differentiate among the three bead types because of spectral overlap.

Spectral Analysis Algorithms. In this section we first describe the mathematical basis for our spectral overlap corrections and then discuss an othonormalization procedure which qualitatively enhances the corrected image. A step-by-step implementation of these algorithms (using *MicroFRET* software) will be described in the following section.

All monochrome images should be background subtracted before spectral overlap corrections are performed. We use the following notation:

$$X_u^y \qquad (1)$$

where X can be substituted by 'D', 'A', or 'F' to indicate an image pixel from one of the monochrome fluorescence images acquired through the Donor, Acceptor or FRET channels. The subscript 'u', can be substituted by '*d*', '*a*' or '*f*' to represent a pixel from either a donor, acceptor or FRET bead in the image. Since there is substantial spectral overlap, more than one bead type can be seen in each unprocessed channel (Fig. 3). The superscript 'y', in the equations below, is replaced by 'b' to indicate that the monochrome image has been background subtracted. We can now write the following ratios:

F_d^b / D_d^b = ratio of FRET channel intensity to Donor channel intensity for a 'pure donor' pixel after background subtraction on each monochrome image. (2)

F_a^b / A_a^b = ratio of FRET channel intensity to Acceptor channel intensity for a 'pure acceptor' pixel after background subtraction on each monochrome image. (3)

These ratios are essentially the fractional 'bleed' of donor and acceptor, respectively, into the FRET channel. They are then used to correct the FRET channel pixel intensities. The pixel in the corrected FRET image (F^c) is given by:

$$F^c = F^b - \left(F_d^b / D_d^b\right) \times D^b - \left(F_a^b / A_a^b\right) \times A^b \quad (4)$$

After background and bleed corrected monochrome images are obtained for each channel, the three images are combined into a composite RGB image. Note that the donor channel is not corrected for acceptor bleed and that the acceptor channel is not corrected for donor bleed because these effects are minimal.

In addition to the bleed correction algorithms given above, the image can be further enhanced by the construction of RGB images based on an orthonormal transformation. This process results in the FRET, acceptor, and donor pixels being pseudocolored by pure primary colors: red, green, and blue respectively.

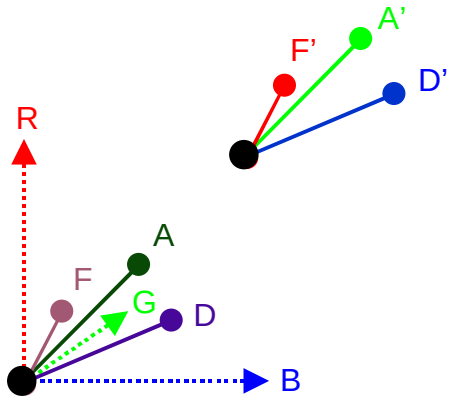

Fig. 4. Orthonormalization of the color axes for an RGB display. This color-correction algorithm redefines the color axes from the dotted arrows of a conventional RGB display (lower left) to the solid axes of the orthonormalized image (upper right). This process results in the primary colors (red, green, blue) being assigned to the three pixel or bead types (FRET, Donor, Acceptor), respectively. Thus, the poorly differentiated colors of the raw RGB image shown in Figure 3 (F, A, and D) are transformed by orthonormalization into pure red (F'), green (A'), and blue (D').

To do this, pixel values from each of the previously processed monochrome images can be used to construct a 3×3 matrix, hereafter referred to as the *A* matrix:

$$\begin{array}{l} \\ \text{Selected Pixel} \end{array} \begin{array}{c} \text{Monochrome Image} \\ \begin{array}{ccc} \text{F} & \text{A} & \text{D} \end{array} \\ \begin{array}{c} \text{f} \\ \text{a} \\ \text{d} \end{array} \begin{bmatrix} A_{11} & A_{12} & A_{13} \\ A_{21} & A_{22} & A_{23} \\ A_{31} & A_{32} & A_{33} \end{bmatrix} \end{array} = [\text{A}] \qquad (5)$$

Columns in [A] represent the three previously processed monochrome images and rows represent selected pixels. For example, A_{11} is equal to a pixel value in the FRET image which corresponds to the location of a FRET bead. A_{12} and A_{13} are equal to the pixel value in the acceptor and donor images, respectively, at this same position.

The goal of the orthonormalization operation is to transform the *A* matrix into the following matrix:

$$\begin{array}{l} \\ \text{Selected Pixel} \end{array} \begin{array}{c} \text{Monochrome Image} \\ \begin{array}{ccc} \text{F} & \text{A} & \text{D} \end{array} \\ \begin{array}{c} \text{f} \\ \text{a} \\ \text{d} \end{array} \begin{bmatrix} C_{11} & 0 & 0 \\ 0 & C_{22} & 0 \\ 0 & 0 & C_{33} \end{bmatrix} \end{array} = [\text{C}] \qquad (6)$$

Where C_{11}, C_{22} and C_{33} are set to the maximum possible pixel value. The transformation can be expressed as follows:

$$[\text{A}]\,[\text{B}] = [\text{C}] \qquad (7)$$

Knowing [A] and [C], the *B* matrix can be determined by multiplying both sides of the equation by the inverse of *A*:

$$[\text{A}]^{-1}\,[\text{A}]\,[\text{B}] = [\text{B}] = [\text{A}]^{-1}\,[\text{C}] \qquad (8)$$

The *A* matrix can be inverted provided the selected pixels define independent axes. Once the *B* matrix has been determined, each RGB pixel value triad is multiplied by the *B* matrix to determine the new triad.

Algorithm Implementation. A composite RGB image has already been described in Fig. 3, and it is reproduced as panel A in Fig. 5. The Fig. 5 panels are magnified so that only the upper left quadrant of the Fig. 3 image is shown.

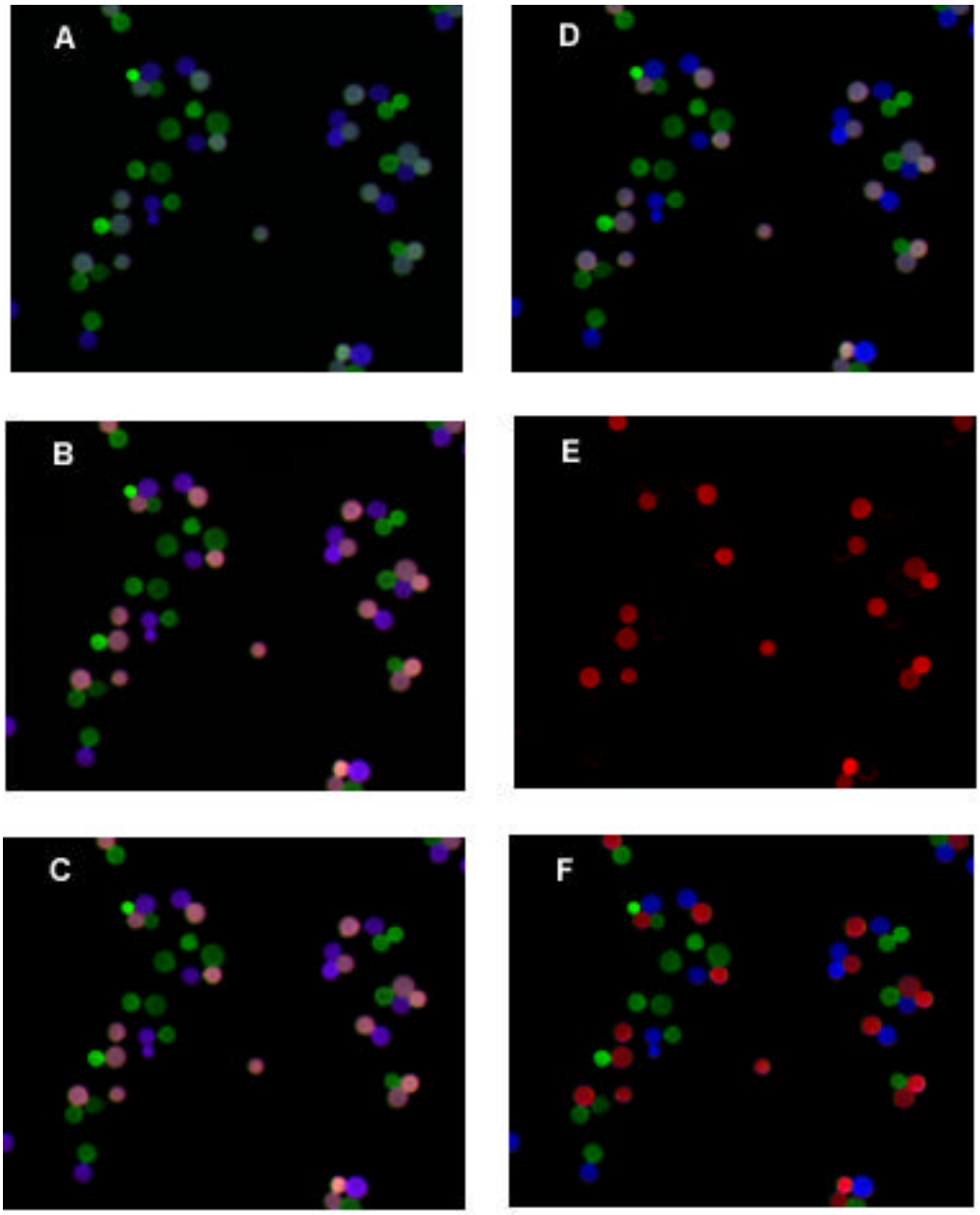

Figure 5. Bleed correction and orthonormalization of donor, acceptor, and FRET beads. A step-by-step description of the panels in this figure is given in the text, below.

Steps in the bleed correction and the orthonormalization of the uncorrected RGB image shown in Fig. 5 (Panels A - F) proceed as follows:

Panel A - RGB. The monochrome images from Figure 3 were combined to generate Figure 5A using D1, A1, and F1 for the blue, green, and red channels, respectively. The color intensity range for all three color channels is based on the minimum and maximum pixel values of the combined three-image set.

Panel B - Scaling corrections. Fluorescence signal intensities among the three channels can vary due to quantum yield and extinction coefficient differences between donor and acceptor. Signal strength will also be dependent on instrument parameters such as illumination intensities of the light source and detector sensitivity at different wavelengths. If the range of pixel values differs significantly between channels, the color of the channel with the highest pixel value readings can overwhelm the color(s) of the channel(s) with lower pixel value readings. Panel B shows the pseudocolor image after individually rescaling the color intensity of each of the three channels to its minimum and maximum pixel values.

Panel C - Background correction. Panel C shows the pseudocolor image after each pixel has been corrected for background signals. *MicroFRET* software prompts the user to select the position of five background pixels by clicking on the image. These pixel values are averaged and automatically subtracted. If any of the subtracted values are negative, they are set to zero.

Panel D - Spectral overlap corrections. The data represented in Figure 3 showed that there is significant spectral overlap among the epifluorescence images. However, because the epifluorescence cubes in the *MicroFRET* instrument maintain precise image registration, the contaminating contributions to the FRET image (and the other images) can be subtracted from all of the pixels. For the FRET channel, this correction is performed according to equation (4) which minimizes donor and acceptor bead pixel values in the FRET channel so that they approach zero. Only pixels from beads performing FRET maintain significant signal intensity in this channel (red) after correction. Panel D shows the pseudocolored image after this overlap correction. The 'red contribution' from the pure donor and pure acceptor beads has been removed. The donor beads now appear blue instead of purple and the acceptor beads now appear as green.

Panel E - Highlighting FRET. To further demonstrate the correction for spectral overlap, we can turn off the green and blue channels in the bleed-corrected image. This process is easily performed in real-time using a simple tabbed dialog box in which each tab allows the user to selectively contrast enhance a particular channel. As can be seen in Panel E, only red beads corresponding to FRET are observed. With very steep contrast enhancement (not advised), artifacts are observed that may be caused by improper image registration.

Panel F. Orthonormalization. In order to enable identification of areas in the sample which contain donor, acceptor, or FRET emission, we have designed software to pseudocolor the image based on user-defined criteria. By clicking the computer mouse on pixels representing each of the three types of beads (i.e., donor, acceptor, and FRET) in Panel D, the user can reset the color assignments to display corrected emission from the donor to pure blue, the acceptor to pure green, and FRET to pure red (Panel F).

We envisage that the othonormalization step will be utilized by cell biologists who may reiteratively select candidate pixels as representatives of the donor, acceptor, and FRET. This human intervention could be a key component in extracting data from images: the quality of the pixel selection would be evaluated by the resulting morphology of the pseudocolored image. For example, if FRET is observed within a particular structure after the spectral overlap correction, it might be advantageous to test various pixels within this structure by re-selecting candidate "red" pixels.

Measurement of donor photobleaching. The maximum extent of photobleaching of the BFP11 donor during a FRET measurement was determined by monitoring the intensity of fluorescence emission from a sample of donor beads which were repeatedly given 30 s exposures to the exciting light (data not shown). The mean pixel value was determined for ten randomly selected pixels after multiple exposures, and these values were compared to the values for the same beads after the initial 30 s exposure. The measured intensity of the fluorescence emission after repeated exposure to the exciting light was >95% of the initial level.

Discussion

Comparison with Earlier Technology. Steady-state FRET imaging of cells by sensitized emission using conventional microscopy has previously suffered from an inability to correct for spectral overlap while maintaining spatial accuracy (Jovin & Arndt-Jovin, 1989; Uster & Pagano, 1986). This is primarily because until now the three epifluorescence cubes (donor, acceptor and FRET) which must be used to generate the correction values have been manufactured with optical surfaces that are not highly parallel. This defect created geometric distortions in the image (i.e., displacement of pixels) after the images are combined. The *MicroFRET* instrument described here employs cubes which have been fabricated to precise tolerances so that spatial co-registration is maintained for all of the images. This new design also makes it feasible to detect relatively small amounts of FRET within a given pixel, because the mathematical correction is much simpler (and therefore more accurate) than was previously possible.

The effectiveness of these corrections was demonstrated by obtaining images of Sepharose beads loaded with either BFP11, RSGFP4, or a defined mixture of the two (which is known to generate FRET). By using these beads as calibration standards, we were able to correct for spectral overlap and identify features within the image displaying donor emission, acceptor emission, and donor-sensitized acceptor emission (FRET). By subsequently applying the orthonormalization algorithm, we were able to pseudocolor the pure donor, pure acceptor, and FRET beads as blue, green, and red, respectively. The latter procedure will be useful to cell biologists who are seeking to determine the spatial distribution of each of these three fluorescent components in tissues and cells.

A second major concern in using the sensitized emission technique has been that the exciting light can photobleach the donor and thereby reduce the apparent intensity of the FRET signal (Uster & Pagano, 1986; Jovin & Arndt-Jovin, 1989). We have measured this variable and have found that it is not likely to reduce the FRET signal by more than 5% when using the proteins and the experimental conditions employed here. One reason that photobleaching does not appear to be a major problem in our system is that broad bandpass filters were used to filter emitted light after excitation with a relatively low power tungsten light source. This should be contrasted with the use of xenon or mercury light sources and narrow bandpass emission filters, a combination of optical components that will result in significantly more light exposure to the sample and photobleaching. The pixel intensities of the fluorescent signals in our experiments, for example, used approximately 1/3 of the total dynamic range of the camera (maximum = 65535 values). Nevertheless, under these exposure conditions, less than 5% of the donor signal was photobleached. The exposure time could easily be reduced by a factor of 10 and still allow the signal to be detected.

Construction of a FRET Bead. While we have focused on the use of the FRET bead as a microscopy calibrant, we have not as yet discussed some of the structure / function aspects of the actual GFP protein bound to the surface of the chelating bead. Because both donor and acceptor GFP molecules are His-tagged, and because GFP can exist as either a monomer or dimer, many different structures can be envisioned on the bead surface (Figure 6). *A priori*, none can be ruled-out; this raises interesting possibilities for constructing other types of beads.

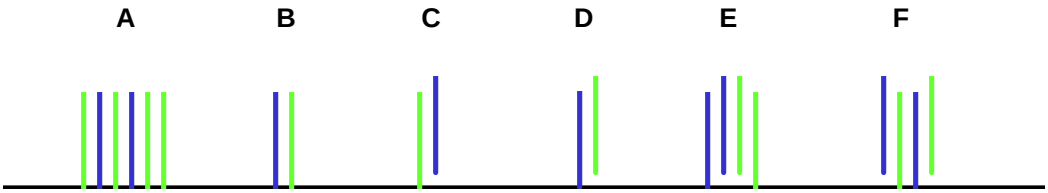

Fig. 6. The surface of the chelating bead is represented by a horizontal black line, GFP donors and acceptors (e.g., BFP and RSGFP) are shown as blue and green vertical lines, respectively. Six different types of possible interactions are labeled A-F and discussed in the text. In this drawing, only adjacent molecules are considered to be within an efficient FRET distance.

As described in the Materials and Methods, prior to binding to beads, both the donor and the acceptor GFPs were premixed at concentrations below levels thought to cause dimerization in solution. In the simplest case, with equimolar mixing and bead saturation, this would result in the binding of monomers in a random order (as depicted in Fig. 6, conformation A). However, if dimer formation did occur prior to bead binding, conformation B is expected. It is also possible that one of the derivatives might have stronger affinity for the bead than the other derivative, resulting in alternative 'heterodimer' structures (C or D). It is even possible that interacting heterodimers could form the actual FRET pair by the two alternative conformations depicted in E and F. Obviously, there are a large number of experimental parameters that could be used to influence which of the possible surface conformations might form.

Future Applications. Although we have demonstrated the capabilities of the *MicroFRET* device by employing a pair of widely used fluorescent protein tags, this system could also be used with non-protein fluorophores such as organic dyes or lanthanide metals, or with combinations of all of these types. We also anticipate an even wider range of applications for this instrument in cell biology studies as more GFP variants with shifted excitation and emission spectra are constructed. Further calibration of the instrument may make it possible to experimentally determine other factors that influence FRET intensity (e.g., the inter-chromophore separation (r), the orientation factor (k^2), and the FRET efficiency (E)). These calibrations may enable the user to create images in which the magnitude and spatial distribution of these coefficients are displayed. Values for the first two variables could be determined by adding, for example, corrections for differences in absorption cross section between donor and acceptor, and corrections for differences in excitation intensity and detector efficiency (Jovin & Arndt-Jovin, 1989). Values for k^2 could be determined by using calibration standards containing chromophores with fixed orientations.

Appendix

The Förster Equations. We have attempted to review the literature on various embodiments of the Förster equations and have found the following composite presentation to be most useful. The basic equations describing this type of energy transfer involve expressions for the energy transfer rate constant (k_t), the transfer efficiency (E), the so-called Förster radius or critical distance (R_0, in cm), the spectral overlap integral (J (λ)) and the normalized fluorescence emission spectrum of the donor (f (λ)) (Förster, 1948,1959; Stryer, 1978; Dörr, 1983; Kuhn, 1983; Herman, 1989; Jovin & Arndt-Jovin, 1989; Cheung, 1991):

$$k_t = (R_0/r)^6 \, (1/\tau_d) \qquad (1)$$

$$E = [1 + (r/R_0)^6]^{-1} \qquad (2)$$

$$R_0 = [8.79 \times 10^{-25} \, J(\lambda) \, \kappa^2 Q_0 n^{-4}]^{-6} \qquad (3)$$

$$J(\lambda) = \int f(\lambda) \, \varepsilon_A(\lambda) \, \lambda^4 \, d\lambda \qquad (4)$$

$$f(\lambda) = F_D(\lambda) \, d\lambda \, / \int F_D(\lambda) \, d\lambda \qquad (5)$$

Here, r is the center-to-center distance (in cm) between the donor and acceptor chromophores, τ_d is the fluorescence lifetime of the donor in the absence of energy transfer, κ^2 is the dipole-dipole orientation factor, Q_0 is the fluorescence quantum yield of the donor in the absence of the acceptor, n is the refractive index of the intervening medium, F_D (λ) is the fluorescence emission intensity of the donor at a given wavelength λ (in cm) and ε_A (λ) is the extinction coefficient of the acceptor chromophore (in $cm^{-1} M^{-1}$). J (λ) therefore expresses the normalized fluorescence spectrum of the donor and has units^2 of $M^{-1}cm^3$. The value of the orientation factor κ^2 can theoretically vary between 0 and 4, but typically $\kappa^2 = 2/3$ for randomly oriented molecules (for a discussion, see Dale & Eisinger, 1975; Stryer, 1978; Herman, 1989; Cheung, 1991). When $r = R_0$, the efficiency of energy transfer is 50%, and the donor fluorescence lifetime is reduced by a factor of 2. Values of R_0 are on the order of tens of Ångstroms (Rosén, 1971). To cite a typical example, R_0 for the fluorescein-tetramethylrhodamine pair is 55 Å (Haugland, 1996).

Other energy transfer scenarios are also possible in which, for example, the acceptor molecule is non-fluorescent or in which a photon is emitted by the donor and simply re-absorbed by the acceptor (trivial energy transfer), but these are not relevant to the conditions (sample geometries and chromophore concentrations) typically present in FRET microscopy experiments (see Weber, 1986).

Acknowledgements

We thank the Department of Energy, Division of Energy Biosciences for supporting basic research on "Macromolecular Scaffolds for Energy Transfer" under DOE DE-FG03-96ER20211.

References

Cheung, H.C. (1991) In: *Topics in Fluorescence Spectroscopy* (Lakowizc, J., ed.) Vol. 2, pp. 127-171, Plenum Press, New York.

Cormack, B.P., Valdivia, R.H. & Falkow, S. (1996) *Gene* **173**:33-38.

Cubitt, A. B., Heim, R., Adams, S.R., Boyd, A.E., Gross, L.A. & Tsien, R.Y. (1995) *Trends Biotechnol.* **20**:448-455.

Dale, R.E. & Eisinger, J. (1975) In: *Biochemical Fluorescence: Concepts* (Chen, R.F. & Edelhoch, H., eds.) Vol. 1, pp. 117-281, Marcel Dekker, New York.

Delagrave, S., Hawtin, R.E., Silva, C.M., Yang, M.M. & Youvan, D.C. (1995) Bio/Technology **13**:151-154.

Dörr, F. (1983) In: *Biophysics* (Hoppe, W., Lohmann, W., Markl, H. & Ziegler, H., eds.) pp.265-279, Springer-Verlag, Berlin .

Förster, T. (1948) *Ann. Physik. (Leipzig)* **2**:55-75.

Förster, T. (1959) *Faraday Soc. Disc.* **27**:1-17.

Haugland, R.P. (1996) *Handbook of Fluorescent Probes and Research Chemicals* (Spence, M.T.Z., ed.) Sixth Edition, p.46, Molecular Probes, Eugene, OR.

Heim, R., Prasher, D.C. & Tsien, R.Y. (1994) *Proc. Natl. Acad. Sci*. *USA* **91**:12501-12504.

Herman, B. (1989) *Methods Cell Biol.* **30**:219-243.

Jovin T. M. & Arndt-Jovin D.J. (1989) In: *Cell Structure & Function by Microspectrofluorometry* (Kohen, E. & Hirschberg, J. G., eds.) pp. 99-117, Academic Press, San Diego.

Kuhn, H. (1983) In: *Biophysics* (Hoppe, W., Lohmann, W., Markl, H. & Ziegler, H., eds.) pp.270-288, Springer-Verlag, Berlin.

Lossau, H., Hummer, A., Heinecke, R., Pöllinger- Dammer, F., Kompa, C., Bieser, G., Jonsson, T., Silva, C. Yang, M.M., Youvan, D.C. & Michel- Beyerle, M. E. (1996) *Chem. Physics*. **213**:1-16.

Mitra, R.D., Silva, C.M. & Youvan, D.C. (1996) *Gene* **173**:13-17.

Prasher, D.C., Eckenrode, V.K., Ward, W.W., Prendergast, F.G. & Cormier, M.J. (1992) *Gene* **111**:229-233.

Rosen, C.-G. (1971) In: *Fluorescence Spectroscopy* (Pesce, A., Rosén, C.-G. & Pasby, T., eds.) pp. 131-147, Marcel Dekker, New York.

Schröck, E., du Manoir, S., Veldman, T., Schoell, B., Wienberg, J., Ferguson-Smith, M.A., Ning, Y., Ledbetter, D.H., Bar-Am, I., Soenksen, D. Garini, Y., and Ried, T. (1996) Science **273**:494-497.

Stryer, L. (1978) *Annu. Rev. Biochem*. **47**:819-846.

Uster, P.S. & Pagano, R. E. (1986) *J. Cell Biol.* **103**:1033-1234.

Weber, G., (1986) In: *Applications of Fluorescence in the Biomedical Sciences* (Taylor, D., Waggoner, A.S., Murphy, R.F., Lanni, F. & Birge, R.R., eds.) pp. 601-615, Alan R. Liss, New York.

Youvan, D.C. & Michel-Beyerle, M.E. (1996) *Nature Biotechnology* **14**:1219-1220.